Time-dependent plane Poiseuille flow
of a Johnson–Segalman fluid

Marios M. Fyrillas[a,b], Georgios C. Georgiou[a,*], Dimitris Vlassopoulos[b]

[a] *Department of Mathematics and Statistics, University of Cyprus, P.O. Box 537, Nicosia 1678, Cyprus*
[b] *Foundation for Research and Technology, Hellas (FO.R.T.H.), Institute of Electronic Structure and Laser,
P.O. Box 1527, Road to Voutes, 71110 Heraklion, Crete, Greece*

Abstract

We numerically solve the time-dependent planar Poiseuille flow of a Johnson–Segalman fluid with added Newtonian viscosity. We consider the case where the shear stress/shear rate curve exhibits a maximum and a minimum at steady state. Beyond a critical volumetric flow rate, there exist infinite piecewise smooth solutions, in addition to the standard smooth one for the velocity. The corresponding stress components are characterized by jump discontinuities, the number of which may be more than one. Beyond a second critical volumetric flow rate, no smooth solutions exist. In agreement with linear stability analysis, the numerical calculations show that the steady-state solutions are unstable only if a part of the velocity profile corresponds to the negative-slope regime of the standard steady-state shear stress/shear rate curve. The time-dependent solutions are always bounded and converge to different stable steady states, depending on the initial perturbation. The asymptotic steady-state velocity solution obtained in start-up flow is smooth for volumetric flow rates less than the second critical value and piecewise smooth with only one kink otherwise. No selection mechanism was observed either for the final shear stress at the wall or for the location of the kink. No periodic solutions have been found for values of the dimensionless solvent viscosity as low as 0.01. © 1999 Elsevier Science B.V. All rights reserved.

Keywords: Planar Poiseuille flow; Johnson–Segalman model; Time-dependent flow

1. Introduction

Several constitutive equations, such as the Doi–Edwards model with a Rouse relaxation mode [1,2], the Johnson–Segalman model with an added Newtonian viscosity [3–6] and the Giesekus model [3,7–9], predict a nonmonotonic shear stress/shear rate behaviour, in a certain range of their parameters. Nonmonotonic constitutive equations admit multiple weak steady-state solutions in viscometric flows, such as the simple shear and Poiseuille flows. These weak solutions are uncountably infinite and are characterized by an arbitrary number of shear rate discontinuities. In Poiseuille flow, the discontinuities are located near the wall; the fluid in the bulk is slightly sheared and the flow is almost plug, whereas

---

* Corresponding author. Fax: +357-233-9061; e-mail: georgios@pythagoras.mas.ucy.ac.cy

the fluid is strongly sheared near the wall. The formation of the high shear rate layer near the wall can be viewed as apparent slip. Linear stability analyses of the above flows predict that steady-state solutions containing velocity segments corresponding to the negative-slope regime of the shear stress/ shear rate curve are unstable [1,3,7]. Various investigators considered this inherent constitutive instability in order to explain the spurt effects observed during the capillary extrusion of certain polymer melts. The constitutive instability mechanism, however, has been criticized by other investigators who state that slip at the wall plays the most crucial role in the spurt instability. Interesting discussions about the two mechanisms of instability can be found in [10,11].

Some recent experimental observations show that nonmonotonic constitutive equations are appropriate for describing the flow behaviour of wormlike surfactant solutions [12,13]. The circular Couette flow experiments Mair and Callaghan [13] and Decruppe et al. [14] show that above a critical shear rate value the flow is subdivided into two or three layers corresponding to different shear rate regimes. Mair and Gallaghan [13] also carried out NMR pipe flow experiments and found that at high shear rates the flow is separated into two layers; near the wall, the shear rate is high, and the velocity profile is pluglike. The appearance of zones of different shear rates, referred to as *shear banding* [12,14], can be modeled easily with nonmonotonic constitutive equations. The points separating the different zones are the discontinuity points of a stable weak (piecewise smooth) steady-state solution.

Yuan et al. [15] solved the creeping two-dimensional plane Poiseuille flow of a Johnson–Segalman fluid using a Lagrangian/Eulerian simulation technique. They used periodic boundary conditions at the inlet and outlet planes of the flow domain and obtained results for a value of the solvent viscosity corresponding to a nonmonotonic shear stress/shear rate behaviour. They showed results for the start-up flow. Unfortunately, for their velocity profile plots, they used only a few points and therefore, it is not clear whether their method is able to catch the expected shear rate discontinuities. They also noticed that in some cases the solution shows oscillatory character but they did not mention whether oscillations persist or decay. Numerical results showing persistent pressure drop oscillations at fixed volumetric flow rate were also reported by Malkus et al. [6,8]. However, as they pointed out [8], the oscillations might be an artifact of the numerical algorithm, i.e., a consequence of the system being slightly damped. More recently, the existence of periodic solutions was reported by Arts and van de Ven [16].

Español et al. [17] solved the creeping one- and two-dimensional plane shear flows of a Johnson–Segalman fluid with added Newtonian viscosity using a Lagrangian/Eulerian method. Their results for the inception of shear flow suggest that, when the nominal shear rate is in the negative slope region of the constitutive equation, there is only one discontinuity point in the final steady state. This point separates the flow into two layers, of which the one adjacent to the fixed wall is characterized by high shear rates. Their results also show that there exists a selection mechanism for the position of the discontinuity and for the steady-total shear stress; the value of the latter is roughly constant for all nominal shear rates in the negative slope region of the constitutive equation [17]. Greco and Ball [18], based on a variational principle, reported similar results for the creeping circular Couette flow of a Johnson–Segalman fluid. They obtained numerical results with two and three bands at low and high velocities of the rotating cylinder, respectively, and observed a selection mechanism for the final shear stress at the interfaces of the bands into which the flow is separated [18].

Georgiou and Vlassopoulos [19] solved the time-dependent plane shear flow of a Johnson–Segalman fluid using mixed finite elements in space and a fully-implicit scheme in time. Their numerical results

agree with the linear stability findings of Kolkka et al. [3] and show that the stable steady-state solution reached in each case and the number of the discontinuity points depend strongly on the initial perturbation. Spenley et al. [12] reached the same conclusion after solving the shear flow of a fluid obeying the 'toy equation' which is nonmonotonic as well. The calculations of Georgiou and Vlassopoulos [19] for the inception of simple shear flow at zero Reynolds number have not revealed the existence of any selection mechanisms, neither for the position of the discontinuity point nor for the final value of the total shear stress; they are, thus, in disagreement with the results of Español et al. [17].

In this paper, we extend the work of Georgiou and Vlassopoulos [19] to the one-dimensional plane Poiseuille flow of a Johnson–Segalman fluid with added Newtonian viscosity. Our objective is to study the dynamics of the flow and investigate whether there exist selection mechanisms for the position of the discontinuity points (kinks) and for the pressure gradient (i.e., the shear stress at the wall), when the volumetric flow rate is in the regime of multiple steady-state solutions. The governing equations and the boundary conditions of the flow are presented in Section 2. In Section 3, we obtain the steady-state solutions. The constitutive equation is nonmonotonic for values of the dimensionless solvent viscosity less than 1/9. In such a case, beyond a critical volumetric flow rate, there exist infinite piecewise smooth solutions, in addition to the standard smooth one. Beyond a second critical volumetric flow rate, no smooth solutions exist. The numerical results are presented in Section 4. The stability of the steady-state solutions to small perturbations is investigated. Our numerical calculations agree with the linear stability predictions of Kolkka and co-workers [3,7] – a steady-state solution is unstable if it contains a segment corresponding to the negative slope regime of the shear stress/shear rate curve. The numerical results for the start up of Poiseuille flow at zero Reynolds number do not show the existence of any selection mechanism for the shear stress at the wall (in the unstable regime). The final velocity solution is smooth for volumetric flow rates less than the second critical value and piecewise smooth with only one kink otherwise. As with the simple shear flow [19], no periodic solutions have been found for values of the dimensionless solvent viscosity as low as 0.01. Our conclusions are summarized in Section 5.

2. Governing equations

We consider the time-dependent planar incompressible Poiseuille flow of a Johnson–Segalman fluid with added Newtonian viscosity. The geometry and the boundary conditions of the flow are shown in Fig. 1. The stress tensor T is decomposed into a purely viscoelastic part T_1 and a purely viscous part $T_2 = 2\eta_2 d$, where η_2 is the viscosity of the solvent and d is the rate of deformation tensor. The governing equations are nondimensionalized by scaling the length by the half-width H of the channel (Fig. 1), the velocity by the average velocity V in the slit, the time by H/V and the stress components and the pressure by $(\eta_1 + \eta_2)V/H$, where η_1 is the viscosity of the polymer. The x-momentum equation thus becomes

$$\mathrm{Re}\,\frac{\partial v_x}{\partial t} = \frac{\partial p}{\partial x} + \frac{\partial p}{\partial x} + \frac{\partial T_1^{xy}}{\partial y} + \eta_2 \frac{\partial^2 v_x}{\partial y^2}, \tag{1}$$

where Re is the Reynolds number:

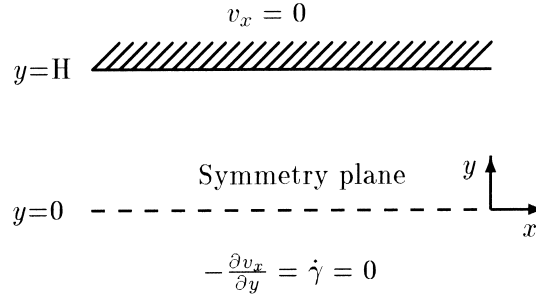$$\mathrm{Re} \equiv \frac{\rho V H}{\eta_1 + \eta_2} \tag{2}$$

$$v_x = 0$$

$$y = \text{H} \quad /\!/$$

Symmetry plane $\quad y$

$$y = 0 \quad \text{-- -- -- -- -- -- -- -- -- -- --}$$

$$x$$

$$-\frac{\partial v_x}{\partial y} = \dot{\gamma} = 0$$

Fig. 1. Geometry and boundary conditions of the planar Poiseuille flow.

and ρ is the density. For the components of $\boldsymbol{T}_1$, in this one-dimensional flow, one gets

$$T_1^{xx} + \text{We}\,\frac{\partial T_1^{xx}}{\partial t} = 2\text{We}\left(1 - \frac{\xi}{2}\right)\frac{\partial v_x}{\partial y}\,T_1^{xy}, \tag{3}$$

$$T_1^{xy} + \text{We}\,\frac{\partial T_1^{xy}}{\partial t} = \eta_1\frac{\partial v_x}{\partial y} + \text{We}\,\frac{\partial v_x}{\partial y}\left[\left(1 - \frac{\xi}{2}\right)T_1^{yy} - \frac{\xi}{2}\,T_1^{xx}\right], \tag{4}$$

$$T_1^{yy} + \text{We}\,\frac{\partial T_1^{yy}}{\partial t} = -\text{We}\,\xi\frac{\partial v_x}{\partial y}\,T_1^{xy}, \tag{5}$$

where We is the Weissenberg number:

$$\text{We} \equiv \frac{\lambda V}{H}, \tag{6}$$

λ is the relaxation time of the polymer, and ξ is a dimensionless material parameter the values of which vary from 0 to 2.

3. Steady-state solutions

In steady state, we get from Eq. (1):

$$T^{xy} = T_1^{xy} + \eta_2\frac{\partial v_x}{\partial y} = T_1^{xy} - \eta_2\dot{\gamma} = -\nabla P\,y, \tag{7}$$

where $\dot{\gamma} = -\partial v_x/\partial y$ is the shear rate and the constant, $\nabla P = -\partial p/\partial x$ is the pressure gradient. (In view of the symmetry boundary condition at $y=0$, the constant of integration is equal to zero and the shear rate is an odd function of y.) From Eqs. (3)–(7), we get

$$T_1^{xy} = -\left[\frac{\eta_1\dot{\gamma}}{1 + 2\xi(1 - \xi/2)(\text{We}\,\dot{\gamma})^2}\right]$$

and

$$T^{xy} = -\left[\eta_2 + \frac{\eta_1}{1 + 2\xi(1 - \xi/2)(\text{We}\,\dot{\gamma})^2}\right]\dot{\gamma} = -\nabla P\,y. \tag{8}$$

For the other two stress components, we obtain

$$T^{xx} = T_1^{xx} = \frac{2(1 - \xi/2)\eta_1 \, \text{We} \, \dot{\gamma}^2}{1 + 2\xi(1 - \xi/2)(\text{We} \, \dot{\gamma})^2} \tag{9}$$

$$T^{yy} = T_1^{yy} = -\frac{\xi\eta_1 \, \text{We} \, \dot{\gamma}^2}{1 + 2\xi(1 - \xi/2)(\text{We} \, \dot{\gamma})^2}, \tag{10}$$

Eq. (8) can be transformed into a cubic equation for $\dot{\gamma}$:

$$\dot{\gamma}^3 - \frac{\nabla P y}{\eta_2}\dot{\gamma}^2 + \frac{1}{\Xi\eta_2}\dot{\gamma} - y\frac{\nabla P y}{\Xi\eta_2} = 0, \tag{11}$$

where

$$\Xi = 2\xi\left(1 - \frac{\xi}{2}\right)\text{We}^2 \tag{12}$$

From the theory of cubic equations, Eq. (11) has three real roots if $\eta_2 < 1/9$. This is the well-known necessary condition for having a shear stress/shear rate curve with a maximum followed by a minimum, as shown in Fig. 2. The three real roots appear only in a certain region of the domain, i.e., when

$$y_{c1} = \frac{1}{\nabla P}\sqrt{\frac{C_1}{\Xi}} \leq y \leq \frac{1}{\nabla P}\sqrt{\frac{C_2}{\Xi}} = y_{c2}, \tag{13}$$
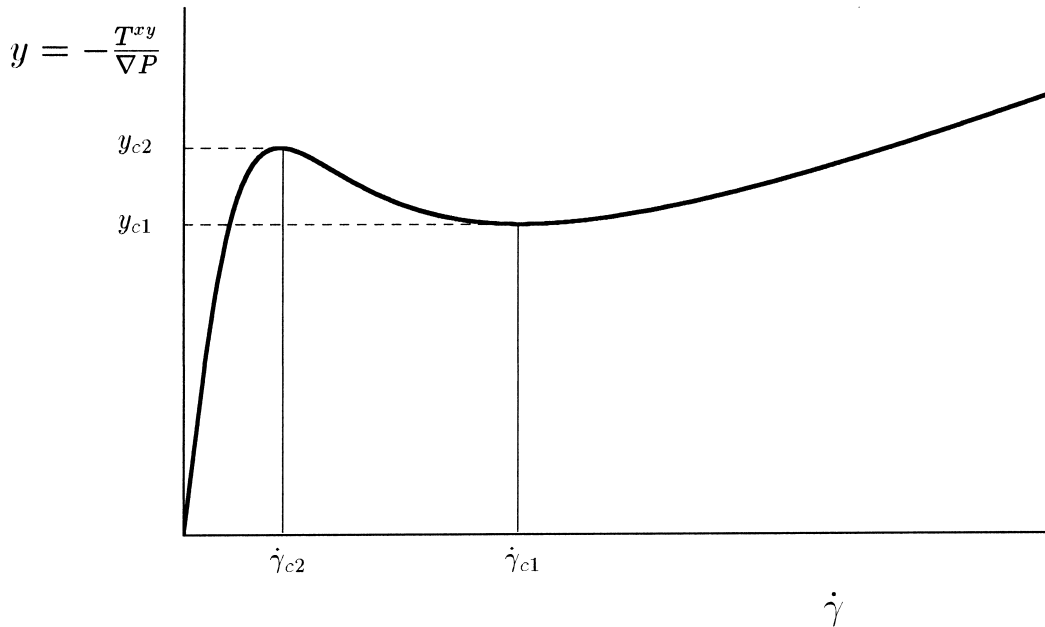

Fig. 2. The value of the ratio $y = -T^{xy}/\nabla P$ as a function of the shear rate $\dot{\gamma}$; $\eta_2 = 0.05$, $\nabla P = 0.8$, $\Xi = 0.36$.

where

$$C_{1,2} = \frac{1 + 18\eta_2 - 27\eta_2^2 \mp \sqrt{(\eta_2 - 1)(9\eta_2 - 1)^3}}{8}. \tag{14}$$

For values of y outside the interval $[y_{c1}, y_{c2}]$, there exists only one real root of Eq. (11). In Figs. 3(a) and (b), we show how the y-range of discontinuous shear rates depends on ∇P and η_2, respectively. The
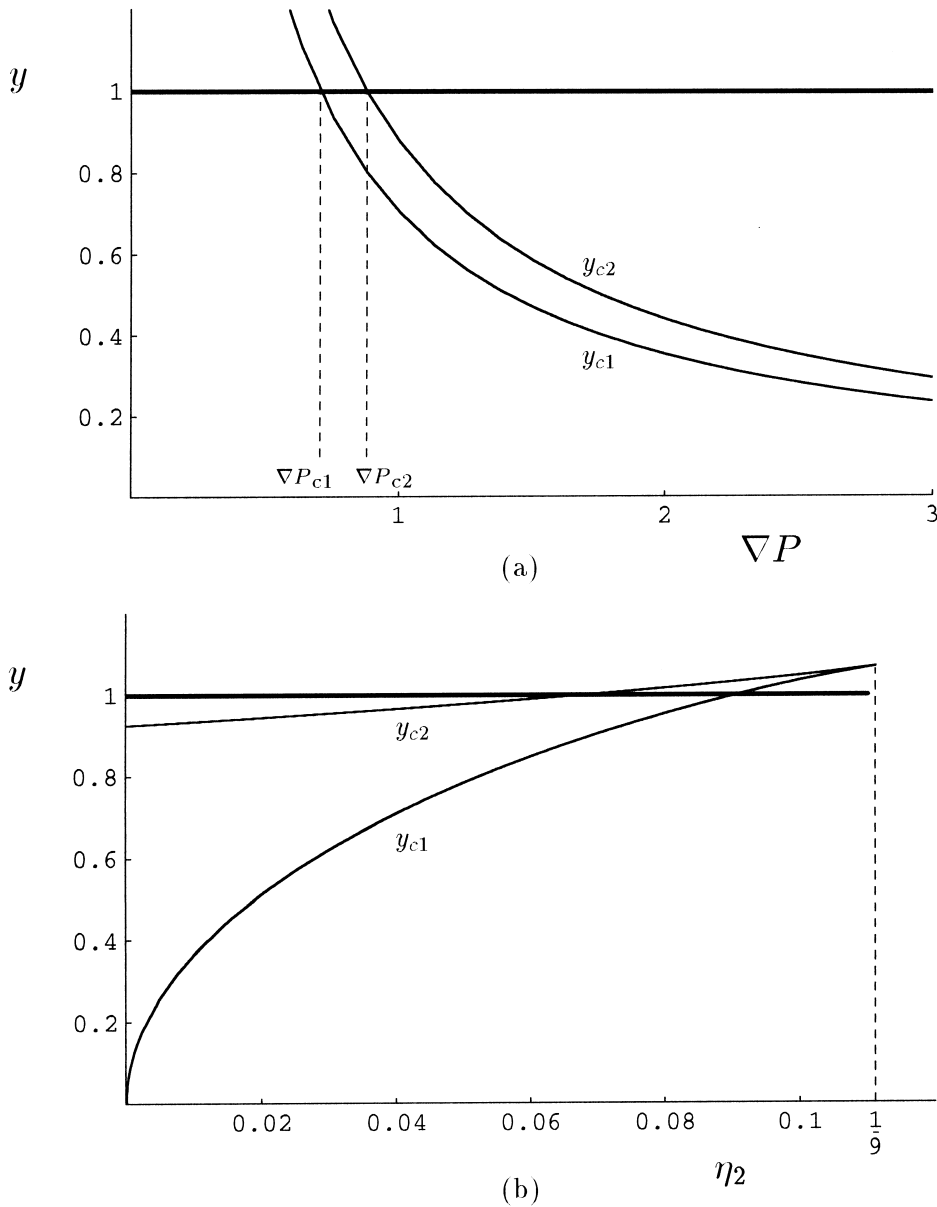

Fig. 3. The range of y values as a function of (a) the pressure gradient ∇P for η_2=0.05 and (b) the parameter η_2 for ∇P=0.9, within which the shear rate is multivalued. We=1, Ξ=0.36.

critical values, ∇P_{c1} and ∇P_{c2} separate the three regions of different behaviour: in $(0, \nabla P_{c1})$ the velocity profile is smooth and unique; in $[\nabla P_{c1}, \nabla P_{c2})$ in addition to the smooth solution, there exist an infinity of piecewise smooth solutions; in $[\nabla P_{c2}, \infty)$ no smooth solution exists. Given that the velocity v_x is obtained by integrating the shear rate $\dot{\gamma}$ from $y=1$ down to $y=0$, we have three distinct cases:

1. If $y_{c1} \geq 1$, there is only one real solution for $\dot{\gamma}$. To obtain v_x, one integrates from $y=1$ to $y=0$ along the left positive-slope branch of the shear stress/shear rate curve. The velocity profile is smooth.
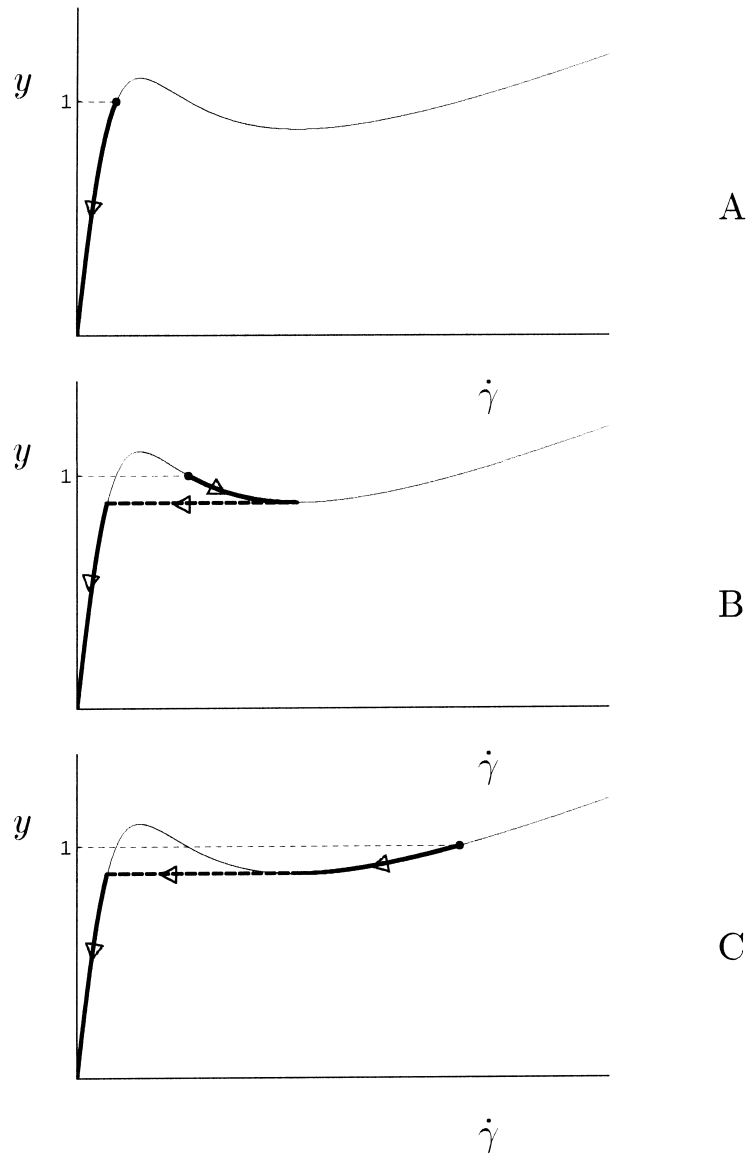
Fig. 4. Three possible ways of integrating the shear rate to obtain the velocity profile for the case $y_{c1} < 1 \leq y_{c2}$; $\nabla P=0.8$, $\eta_2=0.05$, $\Xi=0.36$.

2. If $y_{c1} < 1 \leq y_{c2}$, the situation becomes more complicated. The integration in the interval $[0, y_{c1}]$ is carried out along the left positive slope branch of the shear stress/shear rate curve. More possibilities exist, however, for the integration in the interval $[y_{c1}, 1]$ in which there correspond three real roots of $\dot{\gamma}$. A smooth velocity profile is obtained only if one integrates along the left positive-slope branch (Fig. 4(a)). In all other cases, i.e., if one integrates along the negative-slope branch (Fig. 4(b)) or along the right positive-slope branch (Fig. 4(c)), a jump in $\dot{\gamma}$ will appear at $y = y_{c1}$ and the velocity profile will not be differentiable. The three velocity profiles that correspond to the paths of Fig. 4 are shown in Fig. 5. Note that more jumps from one branch to another are also admissible in the interval $[y_{c1}, 1]$ and thus, the number of the weak steady-state solutions is infinite.

3. If $y_{c1} < y_{c2} < 1$, the integrations from 1 to y_{c1} and from y_{c1} to 0 are carried out along the right and left positive-slope branches of the shear stress/shear rate curve, respectively. As in case (ii), different choices exist for the integration from y_{c2} to y_{c1}. Four of them are illustrated in Fig. 6. In the first three, there is only one jump in $\dot{\gamma}$ and the negative-slope branch of the shear stress/shear rate curve is not used. Using the terminology of Malkus et al. [8], the solutions in Fig. 6(a) and (b) correspond to the top- and the bottom-jumping, respectively. In Fig. 6(d), there are two jumps in $\dot{\gamma}$ and, in some range of y, the integration is carried out along the negative slope branch of the shear stress/shear rate curve. The corresponding velocity profiles are shown in Fig. 7.

As mentioned above, when ∇P exceeds the critical value ∇P_{c1} there exist infinite, piecewise smooth steady-state solutions. The maximum and minimum volumetric flow rates that can be attained correspond to the bottom jumping (Fig. 6(b)) and the top jumping (Fig. 6(a)) scenarios, respectively. The values of ∇P_{c1} and ∇P_{c2} can be obtained by setting y_{c1} and y_{c2} equal to unity in Eq. (13). In Fig. 8, we plot the pressure gradient vs. the volumetric flow rate for the cases of top- and bottom-jumping. For a given value of the volumetric flow rate, the steady-state pressure gradient can be anywhere between the two curves.
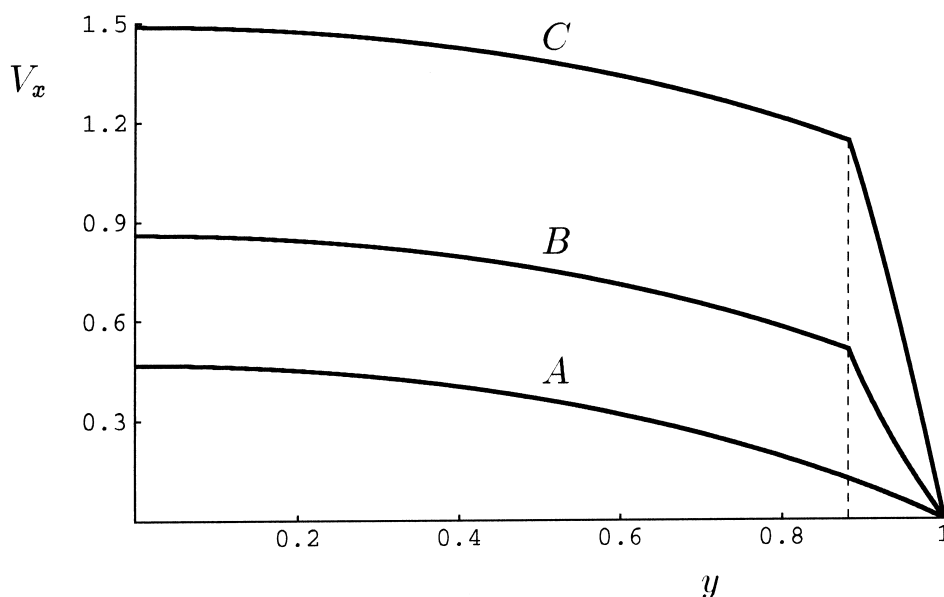

Fig. 5. The velocity profiles obtained by integration of the shear rate along the three paths shown in Fig. 4.
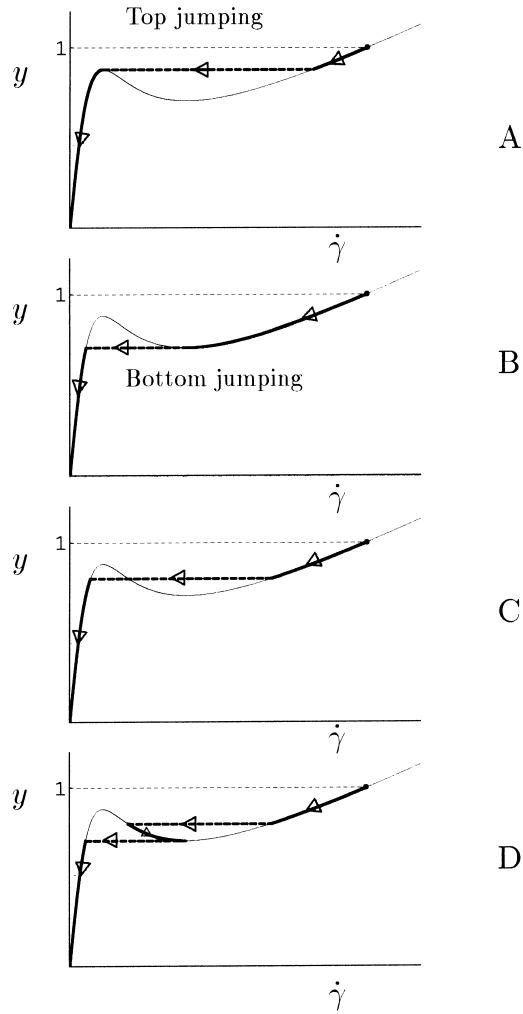
Fig. 6. Four possible ways of integrating the shear rate to obtain the velocity profile for the case $y_{c1} < y_{c2} < 1$; $\nabla P=1.0$, $\eta_2=0.05$, $\Xi=0.36$.

The upper-convected Maxwell fluid ($\eta_2=0$) is a degenerate case and requires better examination. Approximate expressions can be found for the critical pressure gradients by expanding $C_{1,2}$ (Eq. (14)) for small η_2 and substituting in Eq. (13):

$$\nabla P_{c1} \approx 2\sqrt{\frac{\eta_2}{\Xi}}, \quad \nabla P_{c2} \approx \frac{1}{2\sqrt{\Xi}}$$

The results suggest that the branch corresponding to the maximum flow rate shifts to lower pressure gradients. Note that when $\eta_2=0$, there is no branch corresponding to the maximum flow rate (Fig. 8), while the minimum flow rate branch terminates at the critical value $\nabla P = 1/(2\sqrt{\Xi})$. Beyond this critical value, no steady-state solution exists.
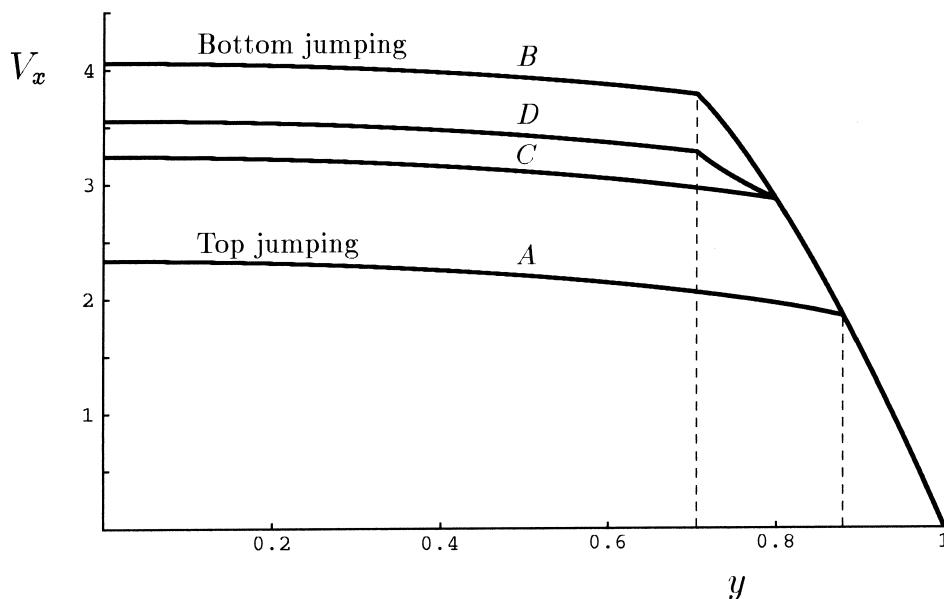
Fig. 7. The velocity profiles obtained by integration of the shear rate along the four paths shown in Fig. 5.

It should be pointed out that the width of the high shear rate layer near the wall gets thinner as the value of η_2 decreases. This is illustrated in Fig. 9, where we show the steady-state velocity profiles corresponding to the top- and the bottom-jumping scenarios for a fixed value of the volumetric flow rate ($Q=0.428$) and various values of η_2. For small values of η_2, the velocity profile might become pluglike. Obviously, numerical simulations for small values of η_2 would require highly refined meshes in order to capture the kink in the velocity profile and attain an acceptable degree of accuracy.

4. Numerical results

In this section, we study the stability of the steady-state solutions presented in the previous section, by solving numerically the time-dependent Eqs. (1)–(5). We use finite elements in space and employ the standard fully-implicit scheme for the time integration. For the viscoelastic part of the stress tensor T_1, we use a zeroth-order approximation in order to avoid the appearance of Gibbs-type oscillations in the numerical solution. For the velocity v_x, we use a biquadratic approximation. All the results presented below have been obtained with a graded mesh of 200 elements; the element size was decreasing geometrically from the centerline to the wall. The size of the element adjacent to the wall was slightly less than 10^{-3}. As for the initial condition, we start form a steady-state solution obtained for a given volumetric flow rate Q_0 and at time $t = \Delta t = 0.0001$ we set the volumetric flow rate equal to a new value Q. The results obtained with the above mesh and $\Delta t=0.0001$ were essentially the same as those obtained with a more refined graded mesh consisting of 400 elements and $\Delta t=0.00001$. The assumption of the volumetric flow rate being constant corresponds to piston-driven incompressible flow. The piston is assumed to be far upstream the domain of interest, and, hence the flow can
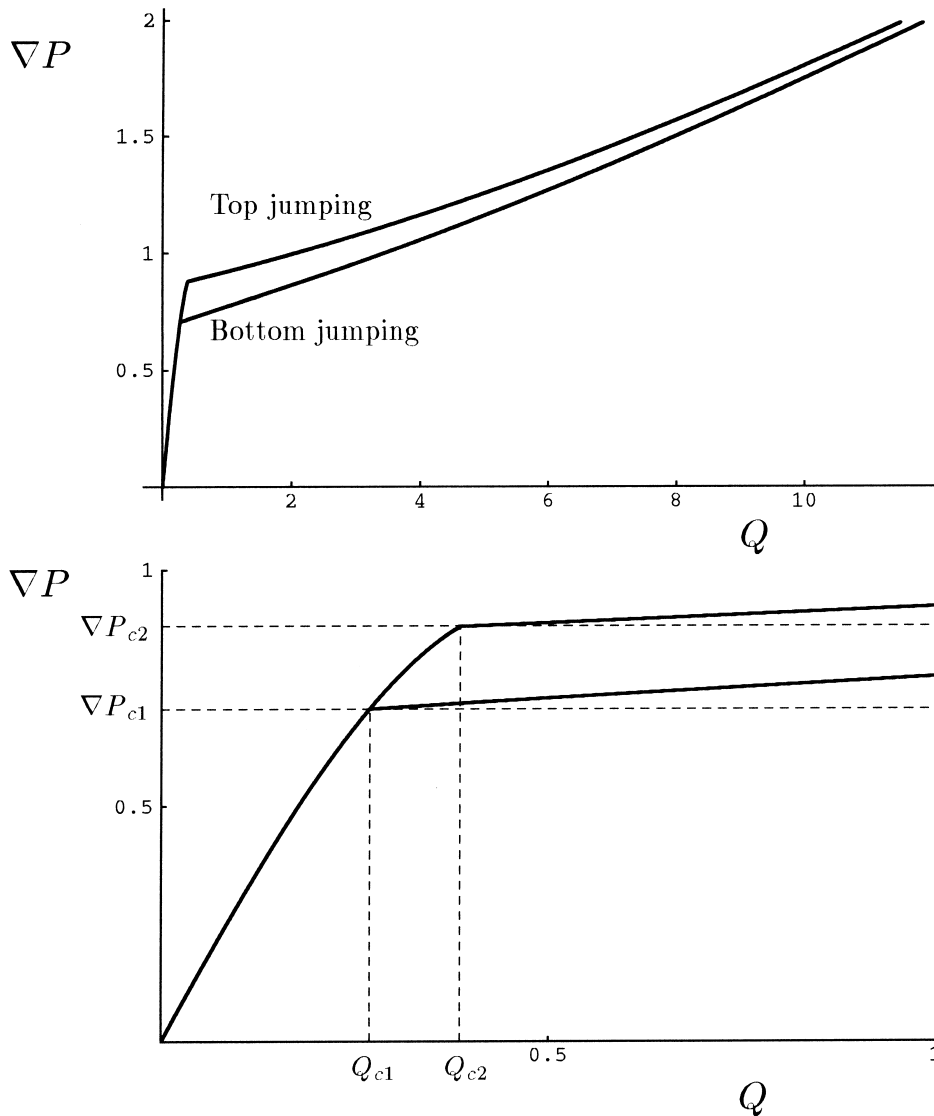
Fig. 8. Top and bottom jumping flow curves. In the region within the two curves there exists an infinity of steady-state velocity profiles with kinks. Figure (b) is a magnification of figure (a) near the origin. The critical pressure gradients $\nabla P_{c1}=0.71$ and $\nabla P_{c2}=0.88$ are calculated with $\Xi=0.36$ and $\eta_2=0.05$. The corresponding critical volume flow rates are $Q_{c1}=0.269$ and $Q_{c2}=0.39$.

be considered fully-developed, i.e., unidirectional. In start-up Poiseuille flow, $Q_0=0$, i.e., the fluid is initially at rest. In all calculations, we have taken We=1, $\eta_2=0.05$, and $\xi=0.2$ unless otherwise stated.

Our time-dependent calculations agree with the linear stability results of Nohel et al. [20] and Kolkka et al. [3]; a steady-state solution is stable to small perturbations if the velocity profile does not contain a convex segment, i.e., a segment corresponding to the negative-slope branch of the shear stress/shear
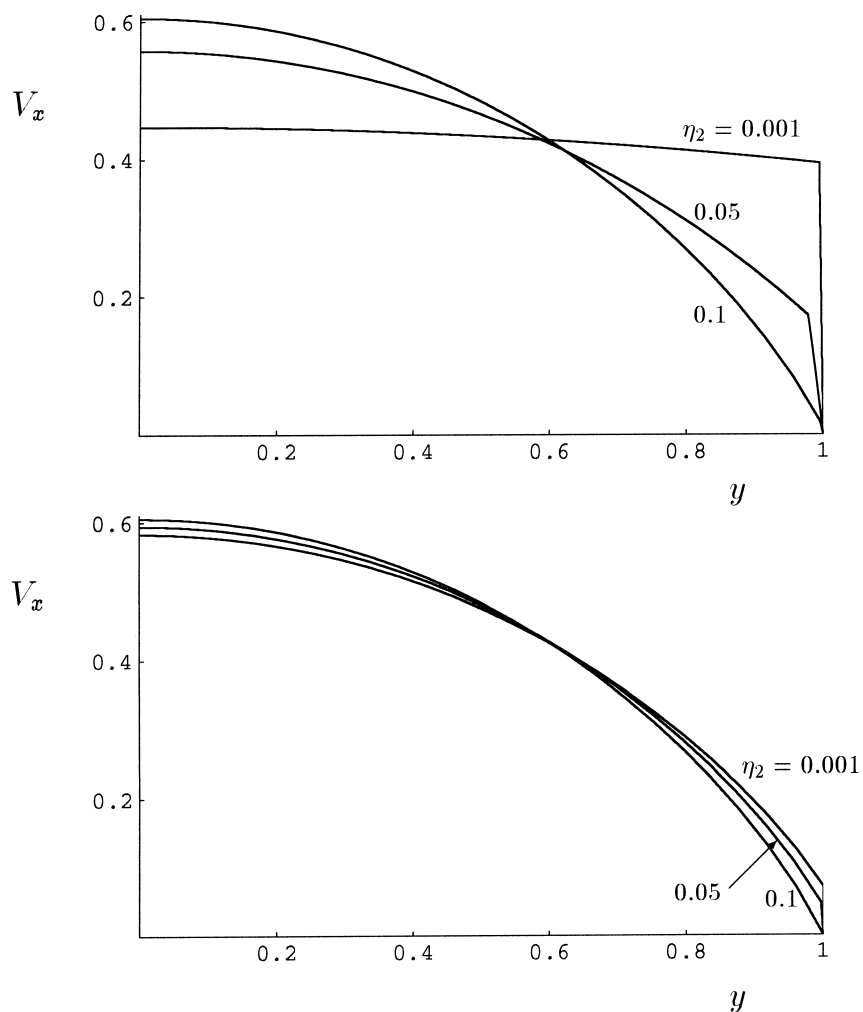
Fig. 9. Steady-state velocity profiles corresponding to (a) bottom jumping and (b) top jumping for various values of η_2. All the profiles correspond to the same volumetric flow rate $Q=0.428$ and $\Xi=0.36$.

rate curve (Fig. 2). Hence, from all the steady-state velocity profiles shown in Figs. 5 and 7, only the profiles B of Fig. 5 and D of Fig. 7 are unstable. In Figs. 10 and 11, we show the time-dependent solutions obtained after slightly perturbing the steady-state solutions corresponding to profiles B and C of Fig. 5, respectively (The volumetric flow rate was perturbed at time $t=\Delta t$ by a small amount of the order of 0.1%.). In the first case, the steady-state solution is unstable. In Fig. 10(a), we show the evolution of the pressure gradient which settles at a higher value than the initial one. In Fig. 10(b), the evolution of the velocity profile is illustrated. A new stable steady-state is reached and the velocity profile has one kink and two concave segments. Note that the new stable steady-state solution is neither top nor bottom jumping. In the second case of profile C, the steady-state solution is stable. As illustrated in Fig. 11, after some oscillations the solution returns to its original form. We also performed numerical calculations starting at different initial conditions, in order to check the effect of the initial
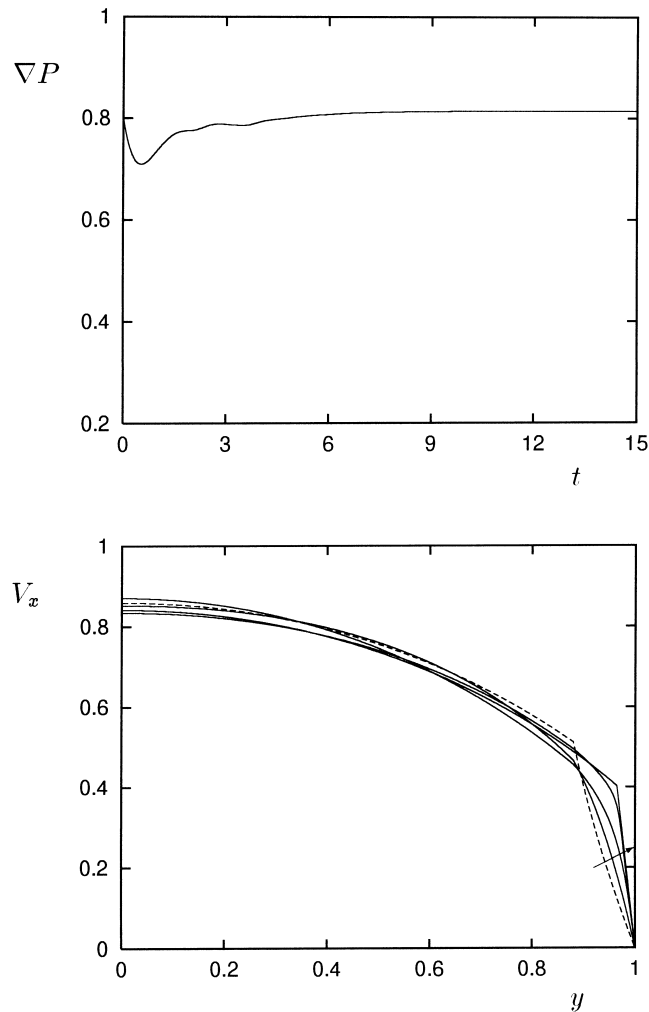
Fig. 10. (a) Evolution of the pressure gradient when the unstable velocity profile B of Fig. 5 is slightly perturbed; (b) Evolution of the velocity profile. The dashed curve is the perturbed steady-state. The model parameters are $\eta_2=0.05$, $\Xi=0.36$, Re=1 and $Q=0.6869$.

perturbation on the final steady state. As in the simple shear flow [19], the initial perturbation determines which of the infinite, stable steady-state solutions will be reached (when the volumetric flow rate is greater than Q_{c1}.

   The next step in our calculations was to investigate whether there exists a selection mechanism for the final pressure gradient (or the shear stress at the wall) in start-up flow. We have thus obtained results for different values of the volumetric flow rate in the three regimes depicted in Fig. 8(b). For values of Q less than Q_{c1}, the unique smooth solution is reached. For values of Q in the interval (Q_{c1}, Q_{c2}), the stable smooth velocity solution is again reached, in spite of the fact that an infinity of stable piecewise smooth steady-state solutions exist in that interval. Obviously, the smooth steady-state solution corresponds to the maximum possible pressure gradient. In Fig. 12, we show the evolution of the
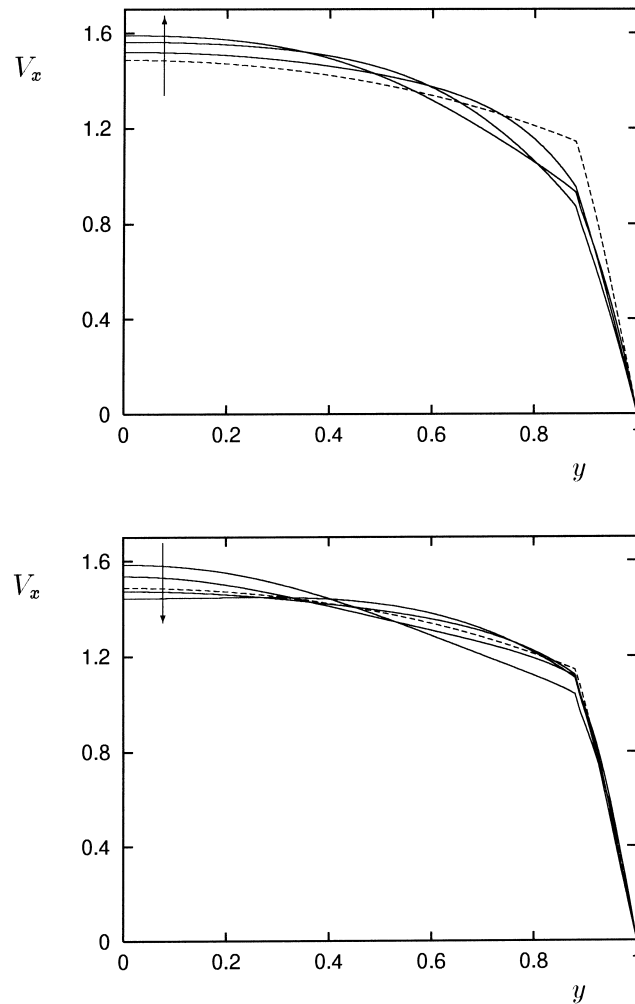
Fig. 11. Evolution of the velocity after a slight perturbation of the velocity profile C of Fig. 5: (a) times from 0 to 0.6; (b) times from 0.8 to 1.4. The final steady-state coincides with the initial velocity and is shown a dashed curve; $\eta_2=0.05$, $\Xi=0.36$, Re=1 and $Q=1.2874$.

velocity profile to the new stable steady-state solution for $Q=0.3216 \in (Q_{c1}, Q_{c2})$ and Re=1. The same calculation was repeated with a smaller Reynolds number, Re=0.01. The same steady-state solution was attained almost immediately; for zero Reynolds number, the stable smooth velocity profile is attained instantaneously when Q is less than Q_{c2}.

For volumetric flow rates above Q_{c2}, no smooth steady-state solutions exist and thus the final steady states reached are piecewise smooth. In all cases examined, the final velocity profile has one kink. In Fig. 13, we plot the evolutions of the pressure gradient and the velocity for a value of Q greater than Q_{c2} and Re=1. In Fig. 14, we plot the final pressure gradient and the final location of the kink versus the imposed value of Q, calculated for the case of creeping flow (Re=0). The final steady state is neither top nor bottom jumping (the asymptotic solution coincides with neither the maximum nor the
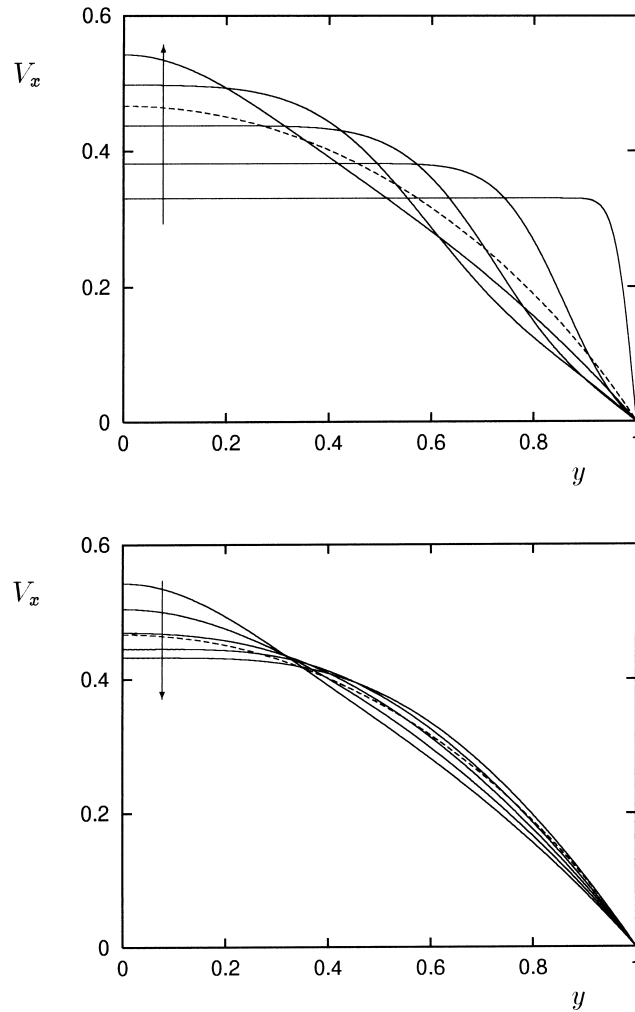
Fig. 12. Transient results for volumetric flow rate $Q=0.3216 \in (Q_{c1}, Q_{c2})$ starting from rest: (a) times from 0 to 0.9; (b) times from 0.9 to 1.4. The dashed curve shows the asymptotic velocity profile which is the corresponding smooth steady-state solution (Fig. 4(a)). The model constants are $\eta_2=0.05$, $\xi=0.2$ and Re=1.

minimum flow rate curves). Furthermore, the results do not suggest the existence of a selection mechanism for the position of the kink nor for the shear stress. In Fig. 13(b), we observe that the time-dependent velocity profile attains a minimum in the centerline for a period of time, a result reminiscent of flows with pulsating pressure gradients [21].

The oscillations of the pressure gradient become larger as the value of η_2 decreases but they are still decaying. Results have been obtained for values of We as high as 5 and values of η_2 as low as 0.01 (Fig. 15). In Fig. 15(b), we plot the velocity profiles corresponding to a minimum and a maximum of the pressure drop. In the latter case, the velocity profile is convex except near the wall, in agreement with the results of Malkus [6]. Unlike his results for $\eta_2=0.007$, however, the pressure drop oscillations are not persistent (Fig. 15(a)). For such small values of η_2, the high shear rate layer near the wall
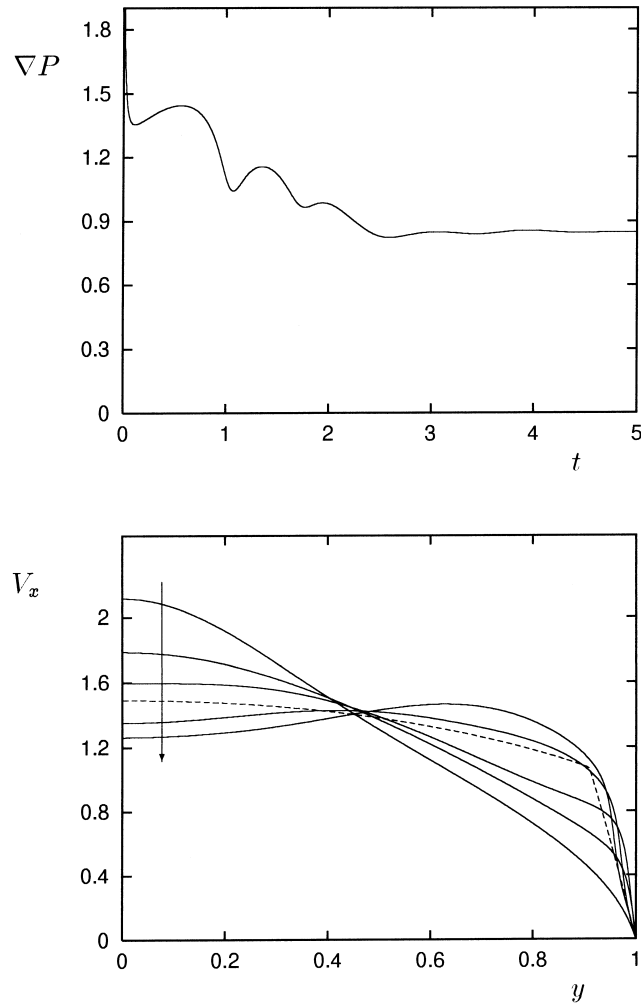
Fig. 13. Transient results for volumetric flow rate $Q = 1.2874 > Q_{c2}$. The model constants are $\eta_2 = 0.05$, $\Xi = 0.36$, and Re=1. The velocity profiles are for times from 0.8 to 1.5. The dashed line is the final steady state.

becomes extremely thin and the flow there cannot be resolved with standard numerical methods and meshes. Let us also note that, for small values of η_2, the negative slope regime of the constitutive equation is large and extends to very high shear rates. This extreme behaviour is not expected physically, since short-relaxation time processes become important causing the stress to increase [12].

5. Conclusions

The stability of the one-dimensional plane Poiseuille flow of a Johnson–Segalman fluid with added Newtonian viscosity has been investigated by means of numerical calculations. When the dimensionless solvent viscosity is less than 1/9, the constitutive equation is nonmonotonic and
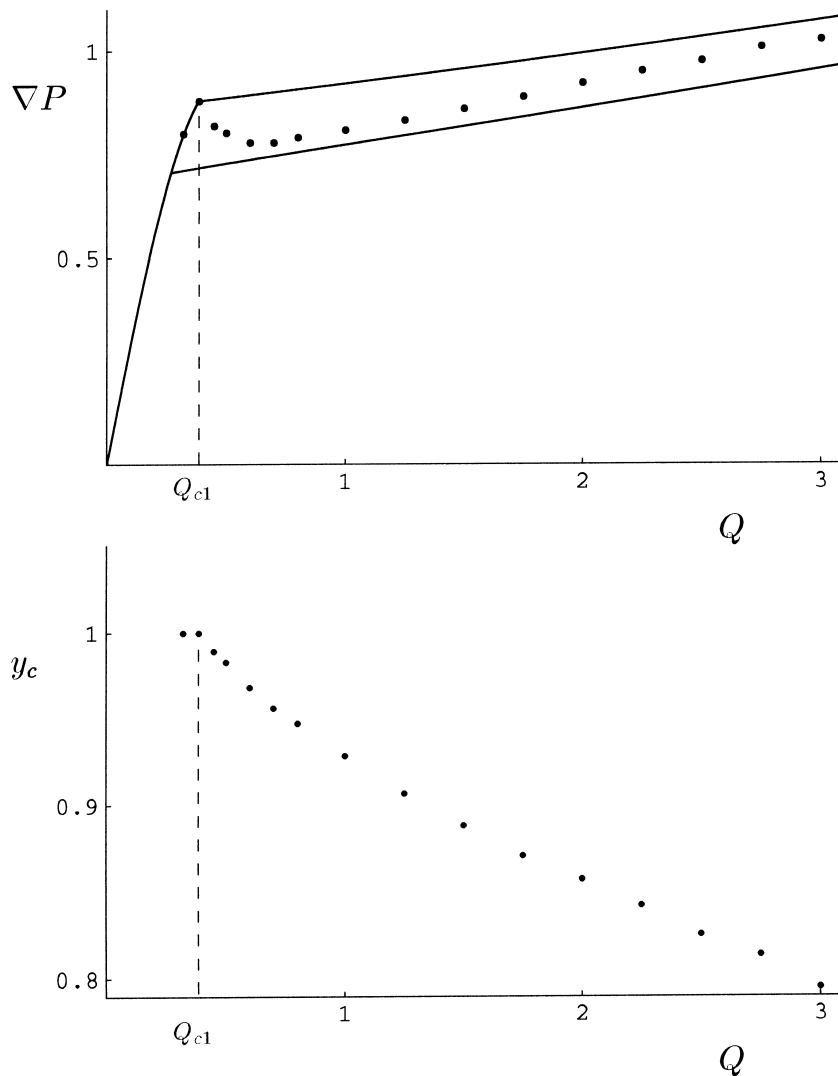
Fig. 14. The final pressure gradient and the final location of the kink attained in constant volumetric flow rate experiments starting up from rest. The model constants are $\eta_2=0.05$, $\Xi=0.36$, and Re=0.

uncountably infinite piecewise smooth steady-state solutions are admitted beyond a critical volumetric flow rate. Steady-state solutions corresponding to velocity profiles with convex segments are unstable, in agreement with linear stability analysis. The time-dependent solutions for start-up Poiseuille flow converge to a smooth velocity profile in case such a solution exists; else, a piecewise-smooth velocity profile with one discontinuity point near the wall is reached. Our numerical calculations have not revealed any selection mechanisms either for the final value of the pressure gradient or for the location of the discontinuity point. Oscillations of the pressure drop were observed in many occasions, but they were always decaying. Thus, the nonmonotonicity of the constitutive equation alone cannot explain the extrusion instabilities observed experimentally.
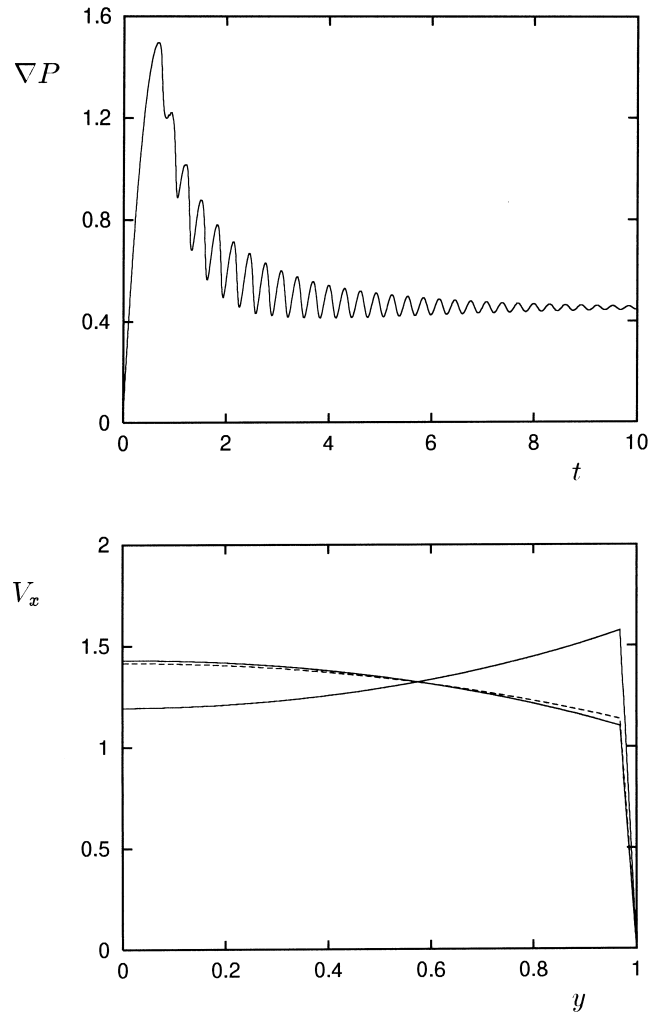
Fig. 15. Transient results for volumetric flow rate $Q=1.3>Q_{c2}$. The model constants are $\eta_2=0.01$, $\Xi=0.36$, and Re=0. The dashed line is the final steady state. The convex profile is at time 3.8 when pressure is at a minimum. The other profile is at time 4.0 when the pressure is at a maximum.

Acknowledgements

References

[1] T.C.B. McLeish, R.C. Ball, J. Polym. Sci. B 24 (1986) 1735–1745.
[2] T.C.B. McLeish, J. Poly. Sci. B 25 (1987) 2253–2264.

[3] R.W. Kolkka, D.S. Malkus, M.G. Hansen, G.R. Ierley, R.A. Worthing, J. Non-Newtonian Fluid Mech. 29 (1988) 303–335.

[4] D.S. Malkus, J.A. Nohel, B.J. Plohr, J. Comput. Phys. 87 (1990) 464–487.

[5] D.S. Malkus, J.A. Nohel, B.J. Plohr, in: Numerical Simulation of Non-Isothermal Flow of Viscoelastic Liquids, J.F. Dijksman, G.D. Kuiken (Eds.), Kluwer, Dordrecht, 1993, pp. 57–71.

[6] D.S. Malkus, RRC144, University of Wisconsin, Madison 1997.

[7] R. Kolkka, G. Ierley, J. Non-Newtonian Fluid Mech. 33 (1989) 305–323.

[8] D.S. Malkus, J.A. Nohel, B.J. Plohr, in: Proc. IUTAM Symp. on Numerical Simulation of Non-Isothermal flow of Viscoelastic Fluids, vol. 28, 1993, pp. 57-71.

[9] D. Vlassopoulos, S. Hatzikiriakos, J. Non-Newtonian Fluid Mech. 57 (1995) 119–136.

[10] Y.-L. Chen, R.G. Larson, S.S. Patel, Rheol. Acta 33 (1994) 243–256.

[11] K.E.P. Adewale, A.I. Leonov, Rheol. Acta 36 (1997) 110–127.

[12] N.A. Spenley, X.F. Yuan, M.E. Cates, J. Phys. II. France 6 (1996) 551–571.

[13] R.W. Mair, P.T. Callaghan, J. Rheol. 41 (1997) 901–924.

[14] J.P. Decruppe, R. Cressely, R. Makhloufi, E. Cappelaere, Colloid Polym. Sci. 273 (1995) 346–351.

[15] X.F. Yuan, R.C. Ball, S.F. Edwards, J. Non-Newtonian Fluid Mech. 46 (1993) 331–350.

[16] A.C.T. Aarts, A.A.F. van de Ven, in: H. Neurzert (Ed.), Progress in Industrial Mathematics at EMCI94, Wiley, Chichester, 1996, pp. 216–223.

[17] P. Español, X.F. Yuan, R.C. Ball, J. Non-Newtonian Fluid Mech. 65 (1996) 93–109.

[18] F. Greco, R.C. Ball, J. Non-Newtonian Fluid Mech. 69 (1997) 195–206.

[19] G.C. Georgiou, D. Vlassopoulos, J. Non-Newtonian Fluid Mech. 75 (1998) 77–97.

[20] J.A. Nohel, R.L. Pego, A.E. Tzavaras, Proc. Roy. Soc. Edinburgh Sect. A 115 (1990) 39–59.

[21] K.D. Rahaman, H. Ramkissoon, J. Non-Newtonian Fluid Mech. 57 (1995) 27–38.